Energy band alignment for Cd-free antimony triselenide substrate structured solar cells by Co-sputtering ZnSnO buffer layer

Y.-D. Luo, M.-D. Chen, R. Tang, M. Azam, S. Chen, Z.-H. Zheng, Z.-H. Su, P. Fan, H.-L. Ma, G.-X. Liang, et al.

Energy Band Alignment for Cd-free Antimony Triselenide Substrate Structured Solar Cells by Co-sputtering ZnSnO Buffer Layer

Yan-Di Luo[1,2], Ming-dong Chen[1], Rong Tang[1], Muhammad Azam[3], Shuo Chen[1], Zhuang-Hao Zheng[1], Zheng-Hua Su[1], Ping Fan[1], Hong-Li Ma[2], Guang-Xing Liang[*1], Xiang-Hua Zhang[2]

[1]*Shenzhen Key Laboratory of Advanced Thin Films and Applications, Key Laboratory of Optoelectronic Devices and Systems of Ministry of Education and Guangdong Province, College of Physics and Optoelectronic Engineering, Shenzhen University, Shenzhen, 518060, P. R. China*

[2] *Univ Rennes, CNRS, ISCR (Institut des Sciences Chimiques de Rennes) UMR 6226, Rennes, F-35000, France*

[3] *Department of Physics, Faculty of Sciences, University of Central Punjab, Lahore, 54000, Pakistan*

*Corresponding author, E-mail: lgx@szu.edu.cn (Prof. G.X. Liang)

Keywords: Sb_2Se_3; ZnSnO; Band alignment; Magnetron sputtering deposition; Solar cell

Abstract

Antimony selenide (Sb_2Se_3) have developed as an environmental-friendly photoactive materials for low-cost photovoltaics due to its non-toxic elements and excellent optoelectronic properties. However, chemical bath deposited (CBD) CdS thin film was generally employed as electron transport layer (ETL) in substrate or superstrate structured Sb_2Se_3 solar cells, which was still a huge concern restraining its long-term advancement. In this work, we have replaced the toxic CdS film by employing ZnSnO films fabricated through magnetron co-sputtering technique to develop Cd-free ZnSnO/Sb_2Se_3 solar cells. It was observed that Sn/(Zn+Sn) in ZnSnO film affecting the energy band alignment with Sb_2Se_3 take part in improving the device efficiency. Substrate structured Cd-free Sb_2Se_3 based devices with a champion device performance of 3.44%, were firstly made with the optimized $Zn_{0.57}Sn_{0.43}O$ buffer layer closely related to the rational band alignment, the reduced recombination losses at interface (ZnSnO/Sb_2Se_3), and efficient charge transfer. This substituted sputtering ZnSnO for CBD-CdS film demonstrated remarkable potential to efficient and Cd-free Sb_2Se_3 solar cell with full-vacuum process.

1. Introduction

Sb_2Se_3 has gained a tremendous attention for cost-effective, environment friendly, and stable solar cells.[1-4] It possessed extremely attractive properties such as a unique quasi-one dimensional crystal structure, proper optical band gap (1.10-1.30 eV, which approached to the absolute Shockley-Queisser value), [5-8] excellent light absorbance coefficient[9, 10] (>10^5 cm^{-1} in the visible region), and efficient charge carrier mobility.[11, 12] Besides, being a new type of potential material, Sb_2Se_3 is non-toxic and its employment in photovoltaic technologies would avoid the scarcity issue.[13] Additionally, earth-abundant composition and simple fabrication are preferable to low-cost manufacturing. [14-16] Hence, such promising properties build Sb_2Se_3 a potential alternative light absorber to substitute other photoactive materials (CIGS or CdTe) for further improvement in device performance.[17, 18] Nair et al.[19] have employed Sb_2Se_3 as photoactive absorber layer and obtained a comparatively lower power conversion efficiency (PCE) of 0.66%. However, Sb_2Se_3-photoactive based photovoltaic have been substantially researched and acquired significant improvement in the last few years. The highest efficiencies of Sb_2Se_3-based devices are reported to be 7.6% and 9.2% with the superstrated structured Glass/ITO/CdS/Sb_2Se_3/Au[14] and substrate structured Glass/Mo/Sb_2Se_3/TiO_2/CdS/ZnO/ZnO:Al/Ag, [5] respectively. To date, chemical bath deposited CdS thin film was commonly employed as ETL in Sb_2Se_3 solar cells, which was still a huge hurdle in limiting its long-term progress.[20] CdS material itself as well as its film-fabrication process have revealed serious issues connected with human health. In addition to its toxic nature, the shorter band gap (2.4 eV) of CdS thin film

instigated the optical loss in short wavelength response range.[21] Therefore, it is crucial to substituting a larger band gap and green ETL for CdS for further development of Sb_2Se_3-based photovoltaic. Extensive investigation has been carried out to explore an alternative wide band gap ETLs, such as Zn (O, S),[22] SnO_2,[23] ZnO,[24] $Zn_{1-x}Sn_xO$ (ZTO)[25] and Zn-doped TiO_2.[26, 27]

Among these buffer layers, ZTO buffer has been studied for high efficiency CIGS [25, 28] and CZTS [29] solar cells. However, the research on ZTO buffer layer using in Sb_2Se_3 solar cells has been rarely studied. A commonly employed technique for ZTO film deposition is the atomic layer deposition (ALD), [29-31] which is unavoidably linked with the drawbacks of slow deposition rate and expensive precursors for the perspective of mass production at industrial level. Magnetron sputtering is considered to be an efficient technique owing to its lower deposition temperature, excellent compactness of film, high deposition rate and avoidance of liquid-based generated waste. In this work, we develop ZnSnO layers via magnetron co-sputtering method to substitute the hazardous CdS film for ZnSnO/Sb_2Se_3 based devices. The effect of Zn/Sn in ZnSnO film on solar cell (substrate structured Glass/Mo/Sb_2Se_3/ZTO/ITO/Ag) performance and the corresponding charge transfer mechanism were studied systematically.

2. Experimental Section

2.1 Fabrication Process for thin-films and whole Device

Here we have employed Mo-coated glass substrate for the device fabrication. Prior to deposition, the substrates with the size of 2×2 cm were successively cleaned using

sonication in DI water and ethanol each for 10 min with the assistance of ultrasonic cleaning machine, finally rinsed with DI water and blown with N_2 stream. Just after the cleaning process, magnetron sputtering technique was employed for the fabrication of Sb metallic precursor thin film with a highly pure and dense sputtering target. **Figure 1a** gives the schematic illustration of the preparation process. Before performing the sputtering procedure, the experimental parameters, such as, chamber pressure was kept below 7.0×10^{-4} Pa and argon gas flow rate was kept at 42.5 sccm. To ensure the deposition of high-compact thin film, the optimized pressure and sputtering power was conducted at 0.5 Pa and 35 W during the deposition development according to our previous research [31]. Unless otherwise specified, no intentional heating treatment is applied to the samples in this deposition process. The sputtering time was set to be 40 min to obtain Sb metallic precursor thin film with the thickness of 600 nm.

Subsequently, the Sb metallic precursor thin film was subjected to a selenization process to grow high-crystallinity Sb_2Se_3 thin film. As can be seen in **Figure 1b**, two ceramic boats each containing 0.1 g Se powder (>99.99%) and the as-sputtered Sb deposited samples were put into the furnace together. Moreover, the pressure was set to be at 5×10^{-4} Pa during the selenization, operating with a mechanical pump. The selenization process temperature and time were set to be at 410 °C and 15 min, respectively. After finishing the procedure of selenization, the samples were takeout from the furnace and placed at room temperature for some time.

For the deposition of $Zn_{1-x}Sn_xO$ ETL, ZnO and SnO_2 target materials were employed in magnetron co-sputtering process The deposition process can be seen from **Figure 1c**.

Additionally, ZnO and SnO_2 films were also fabricated onto the glass substrates for comparison. The co-sputtering process begins running with the working pressure of 1 Pa. Furthermore, only high purity argon gas was flowed (at 30 sccm) into the vacuum chamber as a sputtering gas for the co-sputtering. The sample holder was rotated at the speed of 30 rpm so as to obtain uniform thin film thickness. The ZTO films composition was controlled via varying theRF-powers of ZnO and SnO_2 targets during co-sputtering. **Table 1** shows the different Sn/(Sn+Zn) were denoted as ZTO1, ZTO2, ZTO3 and ZTO4.

Indium tin oxide (ITO) window layer was sputtered on the ZTO film by a sequential process, using magnetron sputtering with the working parameters of 120 W, 0.4 Pa, a flow rate of 30 sccm and 7 sccm for argon and oxide gas, respectively **(Figure 1d) [Ref]**. To complete device structure, Ag metallic contact was fumed on the ITO film through thermal evaporation. Finally, for small active area of the devices were mechanically engraved into small squares. The active area of the ZTO/Sb_2Se_3 devices is 0.135 cm^2. **Figure 1e** indicates the adopted device structure of prepared Sb_2Se_3-based photoactive thin film (Mo/Sb_2Se_3/ZTO/ITO/Ag). Finally, we successfully obtained the complete Sb_2Se_3 device **(Figure 1f)**.

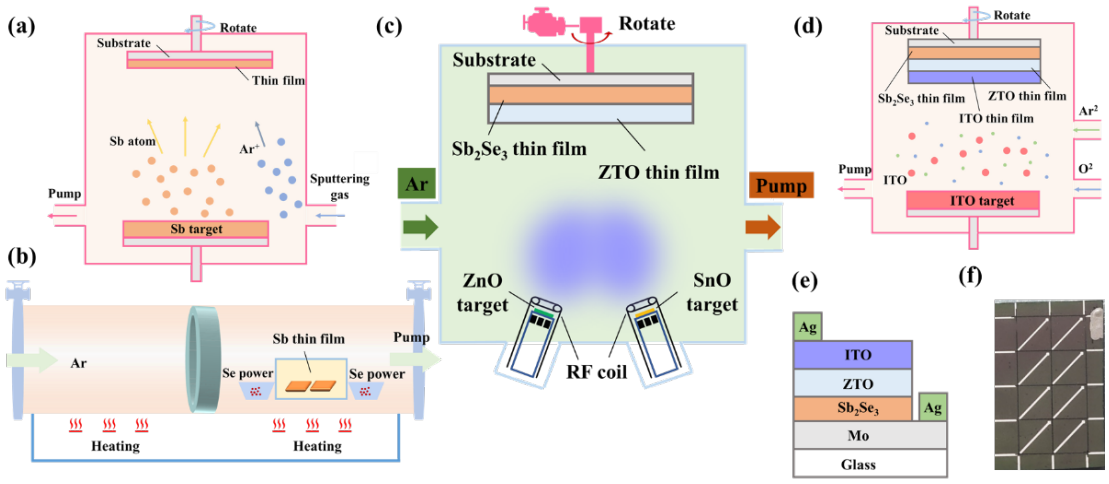

Figure 1. Schematic illustration of the fabrication process of Sb_2Se_3/ZTO thin film solar cell. (a) Sb precursor thin film deposited by RF magnetron sputtering, (b) Sb_2Se_3 thin film obtained by post-selenization heat treatment, (c) ZTO buffer layer deposited via RF magnetron co-sputtering method, (d) ITO layer preparation by magnetron sputtering, (e) Schematic configuration of the final Sb_2Se_3/ZTO thin film solar cell, (f) Practicality image of the final Sb_2Se_3/ZTO thin film solar cell.

2.2. Characterization

Optical performance was measured by a Shimadzu UV/Vis/NIR spectrophotometer. For the convenience of testing, ZTO layer was deposited on bare glass substrates. The cross-section micrograph of whole device with ZTO thin films was observed via emission scanning electron microscope (SEM, ZeissSUPRA 55). The elemental composition of the films was characterized by an energy dispersive X-ray spectroscope (EDS, BRUKER QUANTAX 200). Ultraviolet photoelectron spectroscopy (UPS) analysis was carried out on a domestic Thermal Fisher ESCALAB 250Xi x-ray photoelectron spectrometer with a He I (21.22eV) gas discharge lamp to calculate the energy levels of the ZTO layers. The device performance was characterized using 3A solar simulator under light intensity of 100 mW/cm^2 AM 1.5 G. The external quantum efficiency (EQE)

measurements were conducted with a Zolix SCS101 coupled with Keithley 2400 source meter. Capacitance-voltage (C-V) characterizations were performed at a frequency of 100 kHz and an AC amplitude of 30 mV under dark condition. Drive level capacitance profiling (DLCP) results were obtained using measuring conditions (AC voltage ranges 20 mV to 140 mV and a DC bias voltage from -0.2 V to 0.2 V). Temperature-dependent capacitance-frequency (C-f-T) results were produced by using the frequency range from 1 to 10 kHz. The electrochemical impedance spectra (EIS) were characterized by Zennium electrochemical workstation in the dark condition.

Table 1. Co-sputtering parameters and optical band gap of ZTO films

Sample	Sn/(Zn+Sn)	E_g (eV)	Power ratio ZnO:SnO_2
ZnO	0	3.209	-
ZTO 1	0.29	3.166	8 : 2
ZTO 2	0.38	3.418	6 : 4
ZTO 3	0.43	3.754	1 : 1
ZTO 4	0.56	3.642	4 : 6
SnO_2	1	3.247	-

3. Results and discussion

$Zn_xSn_{1-x}O$ thin films were deposited on glass substrates and the evaluation of Sn/(Zn+Sn) and optical properties were characterized. Figure **2a** showed the transmittance measurements of $Zn_xSn_{1-x}O$ films and the ratio of Sn/(Zn+Sn) is estimated from EDS is given in **Table 1**. A lower cut-off edge at wavelength 450 nm was observed from the transmission spectra of corresponding samples. A small change in transmittance could be attributed to the difference of $Zn_xSn_{1-x}O$ thin film surface

roughness. The optical band gap (E_g) can be acquired using the given relations:

$$\begin{cases} \alpha = d^{-1} ln(T^{-1}) \\ \alpha h\nu = A(h\nu - E_g)^n \end{cases} \quad \textbf{(1)}$$

where d is thickness, and α is the absorption coefficient; T is the transmittance from the measurement. The second relation gives the Tauc plot, in which n is an index related to the nature of the film surface, either it is crystalline or not.[30] Herein, we use n = 0.5 for calculation. **Figure 2b** shows the Tauc plots of ZTO films together with ZnO and SnO_2 films and the band gap is obtained by extending the linear portion of the plot to its X-intercept. The band gap of ZTO can be tuned by different chemical composition through conducting a variety power of ZnO target and SnO_2 target, which the detail parameter is shown in **Table 1**. **Figure 2c** indicates the variation in the band gap as a function of the relative ratio of Sn/(Zn+Sn). On enhancing the Sn ratio in ZTO films, the band gap values were descended from 3.209 f to 3.166 eV for pure ZnO and $Zn_{0.71}Sn_{0.29}O$, respectively, then enhanced again to 3.754 eV for $Zn_{0.57}Sn_{0.43}O$ and finally decreased to 3.247 eV for pure SnO_2. The corresponding band gap value was slightly higher, but the variation trend as a function of Sn/(Zn+Sn) ratio was in good agreement with the previous reports. [32] Thus, it is believed that the optimized Sn concentration would lead to achieving an appropriate band alignment for ZTO/Sb_2Se_3 solar cell.

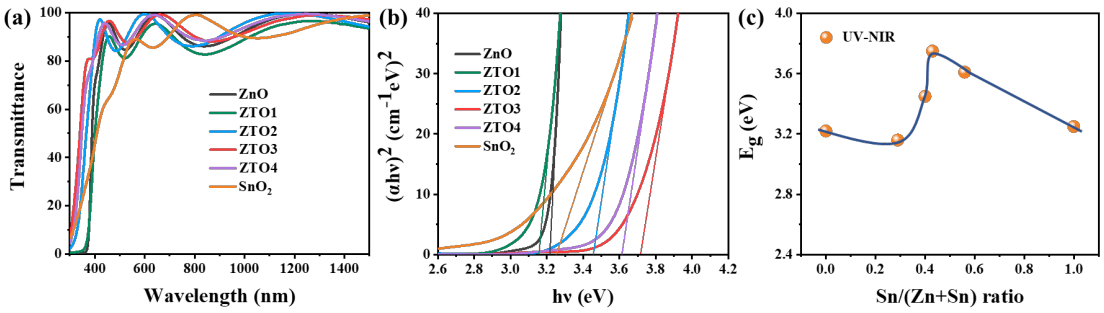

Figure 2. (a) Transmittance spectra of $Zn_xSn_{1-x}O$ films, (b) Tauc plot of $(\alpha h\nu)^2$ versus photo energy ($h\nu$), (c) Optical band gaps extracted from Tauc plot analysis as a function of the relative of Sn/(Zn+Sn).

To further analysis the energy level alignment of multiple layers of whole device, we have carried out UPS measurements. **Figure 3a** exhibits the secondary electron cutoff (SEC) and valance band (VB) spectrum of ZTO films along with ZnO and SnO_2 films. Herein, we have employed following mathematical model (equation 2) to obtain the energy levels (conduction band minimum (CBM) and valence band maximum (VBM)) of corresponding ZTO films: [33]

$$\begin{cases} \psi = h\nu - SEC \\ VBM = \psi + VB \\ CBM = VBM - E_g \end{cases} \quad \textbf{(2)}$$

where $h\upsilon$ is the ultraviolet photoelectron energy, ψ is the work function, and E_g is the band gap obtained from transmittance measurement. Thus, by analyzing the UPS spectrum and band gap, the energy level diagram of the whole device along with ZnO and SnO_2 films is represented in **Figure 3b**, where the energy levels of Sb_2Se_3 and CdS were acquired from our previous works.[11, 34] To obtain considerable device performance, the CBM alignment of absorber layer with the corresponding CBM of ETL is one of the most indispensable factors.[35, 36] Furthermore, a suitable conduction

band offset (CBO) should be "spike"-like within the range0~0.4 eV.[37, 38] In **Figure 3b**, the CBO offset for the ZTO2 and ZTO3 devices was 0.27 eV and 0.18 eV, respectively. Hence, the short spike at interface would not inhibit the electrons transport. In addition, appreciable VBM edge also assembles ZTO3 a successful hole-blocking film which results in decrement in detrimental non-radiative recombination at the interface. The appropriate band alignment of Sb_2Se_3/ZTO3 heterojunction demonstrated the prepared ZTO3 film to be extremely preferable as an electron capture layer for Sb_2Se_3 based devices.

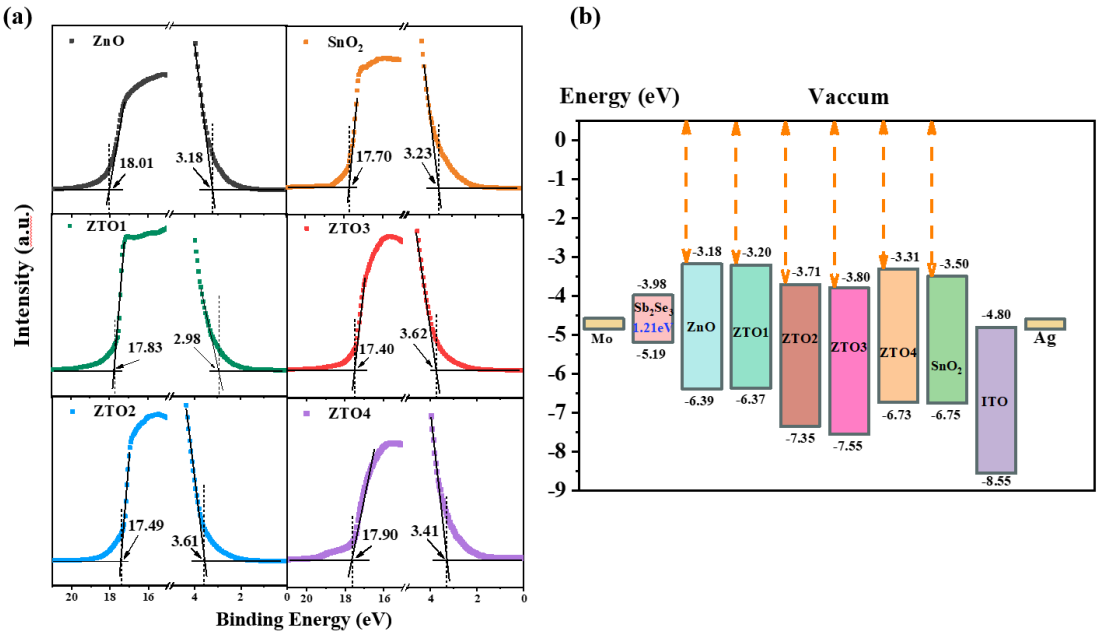

Figure 3. (a) UPS spectra of $Zn_xSn_{1-x}O$ films, (b) A Band gap alignment schematic diagram of the energy band structure of Sb_2Se_3/ZTO device.

To investigate the elemental chemical states of the ZTO thin film, we performed XPS measurements for qualitative and quantitative analysis. The full range XPS spectrum of the ZTO3 revealed the presence of traceable amount of C (**Figure 4a**), which could be assigned to the environmental absorption of quiet a few organics on the surface of the film during sample preparation and/or during the XPS analysis.[36] It is noted that the

occurrence of C peak position conforms to conventional C 1s peak (284.68 eV).[21] Furthermore, the XPS spectrum validates the existence of Zn, O and Sn in the corresponding ZTO film. **Figure 4b**, indicates the two characteristic peaks related to Zn $2p_{3/2}$ and Zn $2p_{1/2}$, located at 1021.6 eV and 1044.7 eV, respectively. The peak of Zn $2p_{3/2}$ is relative to the Zn-O bond in the films.[39] Likewise, as given in **Figure 4c**, the peaks position of the O 1s spectra were fitted by two parts, O-I and O-II, correspondingly centered at 529.8 and 531.0 eV, respectively. The peak of O-I is ascribed to the existence of ZnO_x lattice and O-II is essentially attributed to the O defect states in the thin film, [21, 40] which might be associated with the vacancy defect (V_o), interstitial defect (O_i), or the antisites defect (O_{Zn}). A part from oxygen vacancy generated due to the fabrication process of ZTO3. The photoelectron peaks of Sn $3d_{5/2}$ and Sn $3d_{3/2}$ also were detected at 486.3 eV and 494.7 eV, respectively (**Figure 4d**). The peaks position for Sn matched well with the previously reported work about ZTO.[41] Eventually, the XPS analysis designated the formation of ZTO3 phase by RF co-sputtering method and indicating an efficient authentic technique for the synthesis of environment friendly ZTO films.

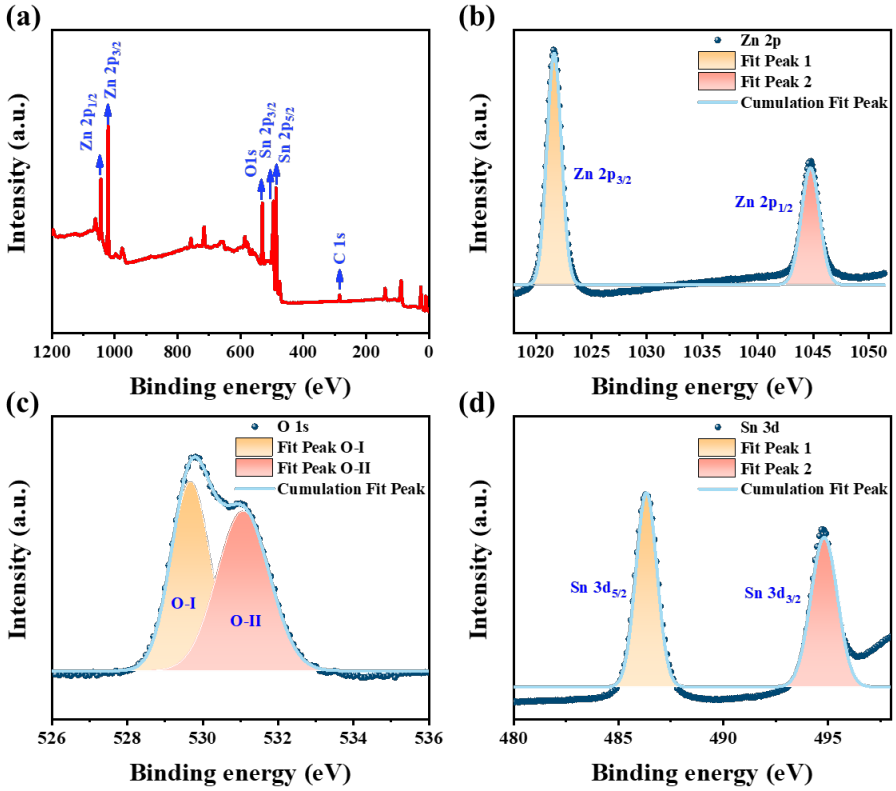

Figure 4. The XPS patterns of ZTO3 film. (a) Full spectrum of ZTO. The peaks of Zn 2p (b), O 1s (c) and Sn 3d orbitals determined by XPS.

Since, the Sb_2Se_3 devices constructed with ZTO1 and ZTO4 exhibited poor performance thus the device characteristics will be restricted to the ZTO2 and ZTO3 based devices. The reproducibility of the devices was investigated by fabricating two batches of the devices (ZTO2 and ZTO3, each containing thirty-five devices) and the statistical analysis of the key solar cells (ZTO2 and ZTO3) performance parameters, containing open circuit voltage (V_{OC}), short-circuit current density (J_{SC}), fill factor (*FF*), and *PCE* are presented in **Figure 5a–d**. The acceptable variation of device performance of the two categories authenticated agreeable reproducibility for these buffer layers and fabrication process. Apparently, the ZTO3 device with slightly larger value of V_{OC}, J_{SC} and *FF* than those of ZTO2, overall confirms a better band alignment of Sb_2Se_3/ZTO

heterojunction of the device. Moreover, the stable performance of the device based on optimized ZTO3 films shows the promising indications for their potential application.

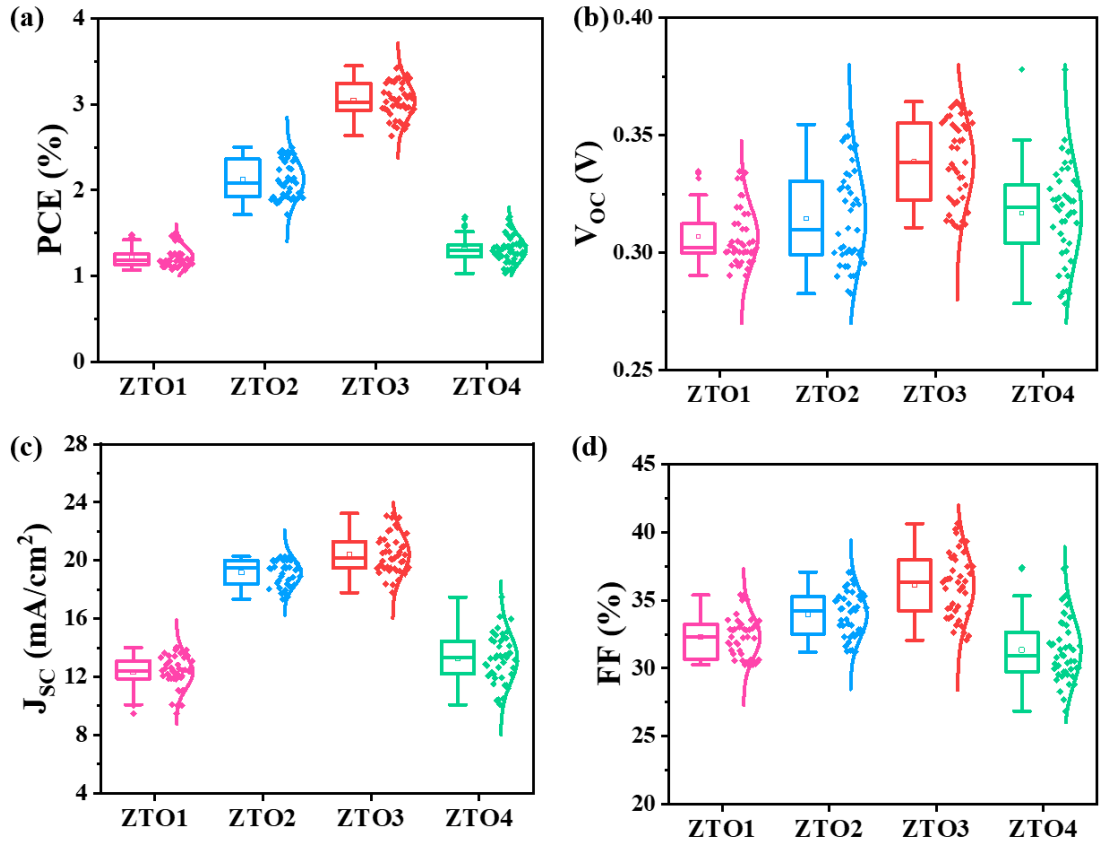

Figure 5. Statistical distribution of the performance parameters including (a) *PCE*, (b) V_{OC}, (c) J_{SC}, and (d) *FF* for ZTO/Sb_2Se_3 devices

Table 2 Device performance parameters of ZTO2 and ZTO3 devices

Sample	*PCE* (%)	V_{OC} (mV)	J_{SC} (mA/cm^2)	*FF* (%)	Integrated J_{SC} (mA/cm^2)
ZTO2	2.50	354	20.26	37.06	19.59
ZTO3	3.44	364	23.23	40.63	22.58

The representative current density-voltage *(J-V)* characteristics and detailed device parameters of Sb_2Se_3 devices are given in **Figure 6a** and **Table 2**. It can be observed that the ZTO2 devices exhibited a J_{SC} of 20.26 mAcm^{-2}, V_{OC} of 354 mV, and *FF* of 37.06%, thus acquiring a *PCE* of 2.50%. On the contrary, ZTO3 device delivered a *PCE*

of 3.44% with an obvious improvement of V_{OC} to 364 mV, J_{SC} to 23.23 mA/cm^2 and *FF* to 40.63%, respectively. Along the better energy band alignment, the improved performance of ZTO3 can also be attributed to large grains of the absorber layer, smooth interfacial boundary, crack-free interface, and strong adhesion between the photoactive and charge extracting films, [11] as shown in the inset in **Figure 6a**. As shown in **Figure 6b**, the EQE analysis of the ZTO2 and ZTO3 devices indicated identical wide photo response within the wavelengths from 300 to 1100 nm, which coincided efficiently with the narrow band gap of Sb_2Se_3. The integrated J_{SC} obtained from EQE results were 19.59 and 22.58 mAcm^{-2} for ZTO2 and ZTO3 devices, respectively. The corresponding integrated J_{SC} values were closely related to the values acquired from J-V measurements **(Figure 6a)**. Importantly, a sharp decline at the range below the wavelength of ~520 nm for cells with a CdS buffer can be observed **(Figure 6b)**. On the contrary, ZTO-buffered solar cell showed significant increasing in EQE values in the spectrum range below ~520 nm. On one hand, the essential EQE improvement is attributed to the employment of wider band gap ZTO thin film as the ZTO-buffered solar cell has a superior blue response in comparison to the CdS-based device.[42] On the other hand, the substantial diminish below 520 nm of CdS-buffered device which could be assign to the absorption of the CdS ETL itself.[43, 44] Larger energy gap value of corresponding ZTO will allow to penetrate large number of photons to the photoactive layer in the wavelength range of ~330 (~3.754 eV) to ~520 nm (~2.4 eV), therefore additional photo-generated charge carriers will be produced in the absorber.[45]

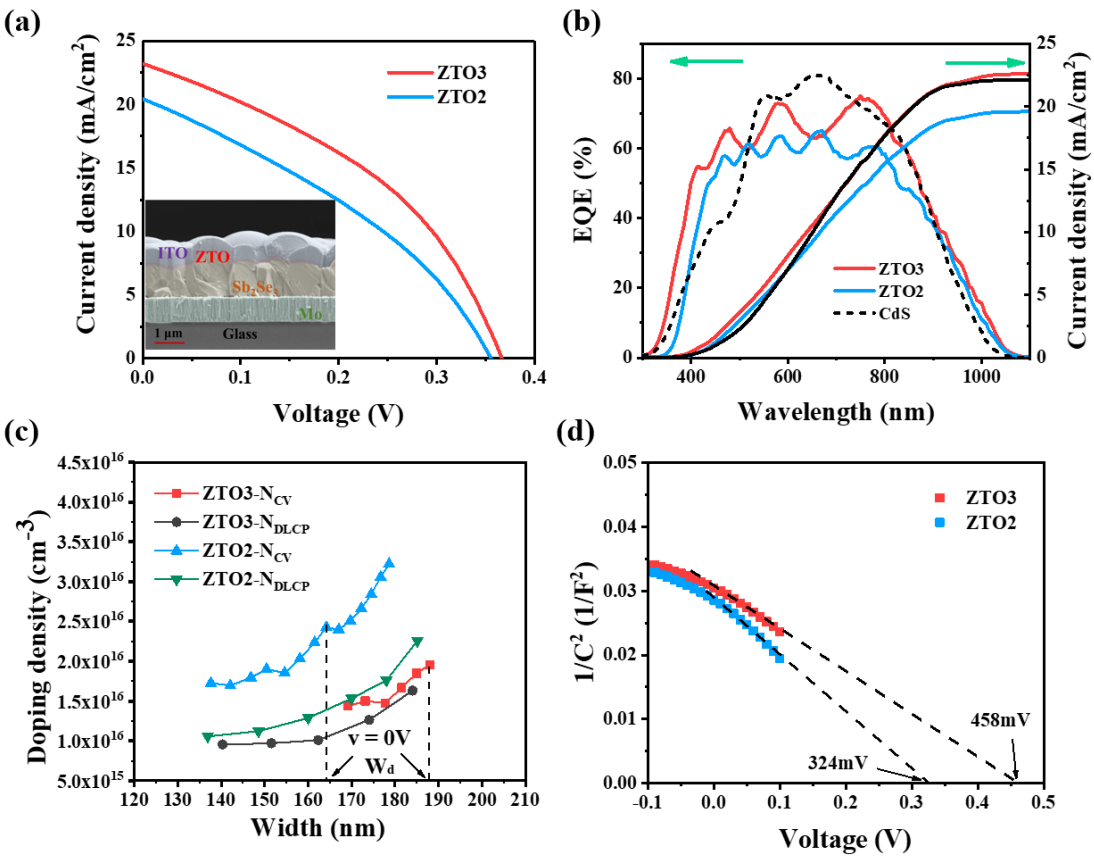

Figure 6. Device performance. (a) Current density-voltage (*J-V*) curves of ZTO2 and ZTO3 devices. (b) External quantum efficiency (*EQE*) and integrated J_{SC} of Sb_2Se_3 devices with ZTO and CdS buffer layers, respectively. (c) doping density profiles and (d) $1/C^2$–V plots of the representative ZTO2 and ZTO3 devices.

Table 3 Doping density calculated from *CV* and *DLCP* of ZTO2 and ZTO3 devices.

	N_{CV} (cm^{-2})	N_{DLCP} (cm^{-2})	Interface defect density (cm^{-2})	Width (nm)
ZTO2	2.43×10^{16}	1.76×10^{16}	6.7×10^{15}	164
ZTO3	1.96×10^{16}	1.63×10^{16}	3.3×10^{15}	188

Moreover, to investigate the interfacial characteristics of the fabricated solar cells (ZTO2 and ZTO3), *C-V* and deep-level capacitance profiling (*DLCP*) characterizations were carried out. Based on the literature, [11, 43] we have calculated the interfacial defect

density ($N_{C\text{-}V}$) and bulk defect density (N_{DLCP}) of the corresponding devices. The respective curves of $N_{C\text{-}V}$ and N_{DLCP} against the profiling depth X (Figure 6c) can be calculated according to the following equation:[46]

$$\begin{cases} N_{C-V} = \dfrac{-2\varepsilon_{r,n}N_D}{\left(\dfrac{d\left(\frac{1}{C^2}\right)}{dV}\right)qA^2\varepsilon_0\varepsilon_{r,n}\varepsilon_{r.p}+2\varepsilon_{r,p}} \\ N_{DLCP} = -\dfrac{C_0^3}{2q\varepsilon_0\varepsilon_{r,p}A^2C_1} \\ x = \varepsilon_0\varepsilon_{r,p}A/C_0 \end{cases} \quad \textbf{(3)}$$

where the parameters N_D, A, ε_0, $\varepsilon_{r,n}$, and $\varepsilon_{r,p}$ are related to the doping density , active area, permittivity of vacuum and the relative permittivity of ZTO and Sb_2Se_3, respectively; whereas, the parameters C_0 and C_1 are obtained from the fitting of C-V plots. It can be clearly seen that there is a large difference between $N_{C\text{-}V}$ and N_{DLCP} curves for ZTO2 in comparison to the device ZTO3, illustrating the ZTO successfully diminish the interfacial defect density and suppress the recombination loss at the Sb_2Se_3/ZTO interface. In addition, the interface defect density could be calculated and summarized in **Table 3**, the value of ZTO2 devices (6.7×10^{15} cm^{-2}) is approximately twice that of ZTO3 devices (3.3×10^{15} cm^{-2}). This result is closely associated to the perfect band alignment of the ETL and absorber layers for the optimized ZTO3 device. Thus, it is assumed that the enhancement in V_{OC} of the ZTO3 device is attributed to the diminished interface defect density. Moreover, it can be observed that the ZTO3 device possesses a slightly larger depletion width (W_d=188 nm) than that of ZTO2 device (164 nm), which indicates a better photon penetration to the absorber and carrier withdrawal capability of the device.

C-V measurements were also carried out to distinguish the interfacial built-in voltage (V_{bi}) of the fabricated ZTO2 and ZTO3 devices. As illustrated in $1/C^2$-V curves **(Figure 6d)**, the V_{bi} values could be evaluated by extracting the curve to X-intercept and linear fitting. The V_{bi} value of ZTO2 and ZTO3 device obtained from $1/C^2$-V curves were observed to be 324 mV and 458mV, respectively. The larger V_{bi} for ZTO3 than that of ZTO2 device, signifying a greatly improved band alignment for ZTO3 device, which validated the results of above *C-V* and *DLCP* analysis.

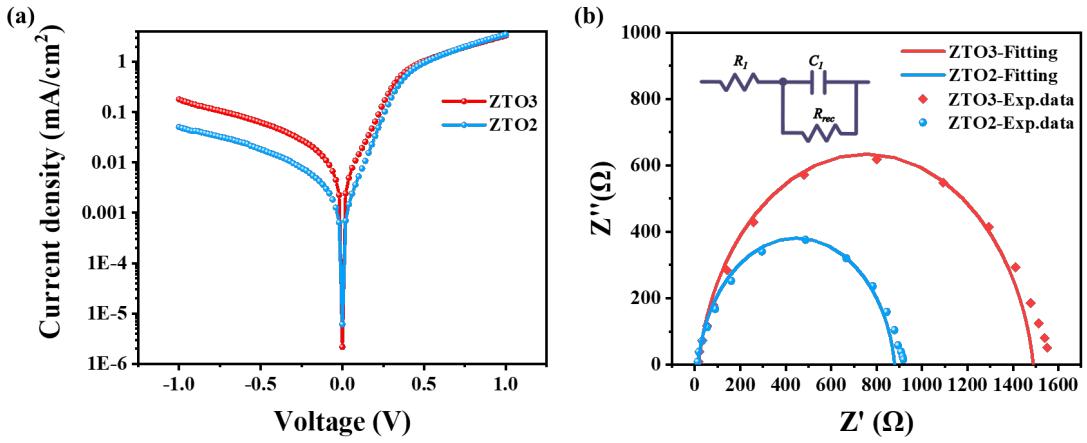

Figure 7. (a) Dark J-V characteristic for ZTO2 and ZTO3 devices, (b) Nyquist plots of the impedance for ZTO2 and ZTO3 devices (inset equivalent circuit employed to fit the Nyquist plots), experimental data are shown as dotted circles and the fitted results are shown as solid lines.

To investigate the electrical behaviors of the representative ZTO2 and ZTO3 devices, dark *J-V* characteristics were estimated. It can be observed from dark current measurements, the ZTO3 device as compared to the ZTO2 displays more competent characteristics and absolutely higher J_{SC}, as given in **Figure 7a**. This specifies that ZTO3/Sb_2Se_3 interface can successfully diminish non-radiative recombination loss and enhance the interfacial contact quality, which result in improvement in device

parameters in terms of J_{SC} and FF. [32, 46] **Figure 7b** presents the electrochemical impedance spectrum at dark condition to examine the interface charge transfer mechanism. As shown in the inset in **Figure7b**, the impedance results were simulated by employing an equivalent circuit model to fit the experimental plot. The fitted results indicated that the recombination resistance (R_{rec}) was obtained to be 846.5 Ω and 1473 Ω for the ZTO2 and ZTO3 device, respectively. In other words, the devices using ZTO3 film as buffer layer show higher recombination resistance, which better obstruct the photogenerated carriers' recombination.

Admittance spectroscopy (AS) has been recognized as a powerful technique to explore the activation energies along with the properties of defect in thin film solar cells.[43, 47] For the sake of further evaluating of the energy distribution of defect density and charge recombination mechanisms of fabricated solar cells, C-f-T analysis were implemented at the temperature vary from 120 to 300 K with steps of 20 K. **Figure 8a** demonstrates the C-f-T spectra of the optimized device (3.44%, ZTO3). The inflection points at different temperatures were obtained by the Arrhenius plot. The corresponding values of inflection point frequency (ω_0) and the defect activation energies (E_a) were extracted from the slopes that were fitted using the following relation: [48]

$$\omega_0 = 2\pi v_0 T^2 exp\left(\frac{-E_a}{kT}\right) \quad \textbf{(4)}$$

where ω_0 is the inflection point frequency, v_0 is the average attempt-to-escape frequency of the defect states, E_a is the energy of defects, which is related to the VBM, which correspond to the average defect energy level in the band gap. [11, 47] According to the capacitance spectra, we obtained two various defect levels labeled as D1 and D2 with

E_a values of 219 meV and 331 meV, respectively (**Figure 8b**).

According to the reported work,[31] the capacity at smaller frequency range is attributed to the result of free charge density and deep level traps, while the capacity at large frequency range is only considered as the result of the response of free charge density. The scattering of defect densities was fitted according to the following reported technique: [43]

$$\begin{cases} E(\omega) = kTln\left(\frac{2\pi v_0 T^2}{\omega}\right) \\ N_t\big(E(\omega)\big) = -\frac{V_d}{qW} \cdot \frac{dC}{d\omega} \cdot \frac{\omega}{kT} \end{cases} \quad \textbf{(5)}$$

where the E is the energy of defects with respect to the VBM, V_d denotes the built-in voltage, ω is the angular frequency, and $N_t(E(\omega))$ is related to the trap states density at the interface. In **Figure 8c-d**, the defect density distribution spectra of D1 and D2 are Gaussian fitted to overlap the plots of N_t versus $E(\omega)$, and the extracted values of defect density were 3.45×10^{15} cm^2eV^{-1} and 5.31×10^{16} cm^2eV^{-1} for the defect type of D1 and D2, respectively. The defect density of optimized device is larger than that of the Sb_2Se_3-based devices with improved performance in previous work, [11, 43] which indicates that there are more deep-level defects in the bulk and interface of the device in this work. That is almost likely to act as recombination centers and causes serious recombination losses, which significantly deteriorate the performance of the device. Briefly speaking, based on the previous discussion, we found that the crucial Sb_2Se_3/ZTO buffer layers interfaces with a few defects (interface engineering) as well as the quality of ZTO film are extremely essential to further enhance the device efficiency.

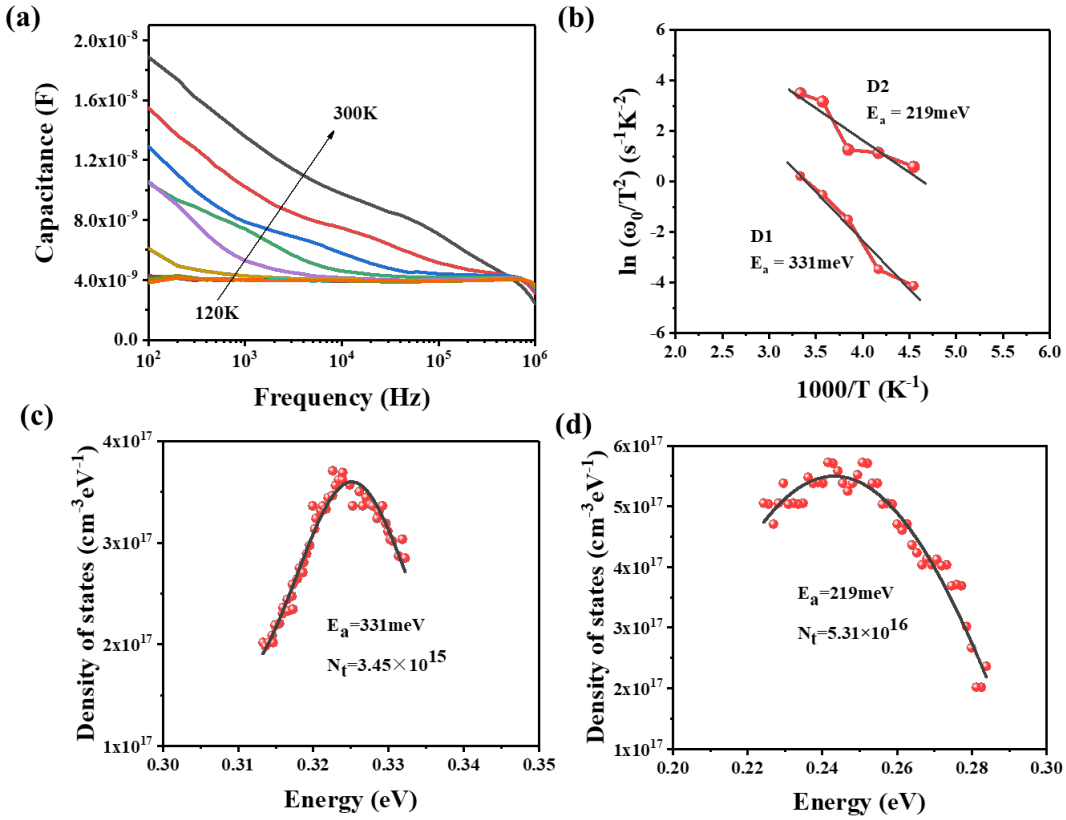

Figure 8. (a) Temperature-dependent admittance measurements of the champion device. (a) Capacitance-frequency-temperature (C-f-T) spectra, (b) Defect activation energies of the ZTO3 device. Defect distributions of D1 (c) and D2 (d) of the ZTO3 device derived from the admittance spectra.

4. Conclusion

A RF magnetron co-sputtering technique has been employed for the deposition of $Zn_{1-x}Sn_xO$ ETLs to fabricate Cd-free substrate structured Sb_2Se_3 based devices. The ratio of Zn and Sn in ZnSnO film influencing its optical band-gap and energy level matching with Sb_2Se_3 played a significant role for the performance of the device. Sb_2Se_3-based devices with configuration Glass/Mo/Sb_2Se_3/ZTO/ITO/Ag were firstly developed with the optimized $Zn_{0.57}Sn_{0.43}O$ buffer layer, demonstrating an interesting efficiency of 3.44%, which is closely related to the band-gap energy of 3.754 eV, the optimized

conduction band offset of 0.18 eV with the spike-like band alignment to Sb_2Se_3, the reduced recombination losses at heterojunction interface, and effective charge transport across the interfaces of the device. This sputtering ZnSnO film demonstrated remarkable potential to Cd-free and efficient Sb_2Se_3 solar cell with full-vacuum process.

Acknowledgements

This work was supported by National Natural Science Foundation of China (No. 62074102), China; Key Project of Department of Education of Guangdong Province (No. 2018KZDXM059), China, China; Science and Technology plan project of Shenzhen JCYJ20190808153409238, China.

Reference

[1] C. Liu, K. Shen, D. Lin, Y. Cao, S. Qiu, J. Zheng, F. Bao, Y. Gao, H. Zhu, Z. Li, Y. Mai, Back Contact Interfacial Modification in Highly-Efficient All-Inorganic Planar n-i-p Sb_2Se_3 Solar Cells. *ACS Appl. Mater. Interfaces 12* **(2020)** 38397-38405.

[2] T. Liu, S. Chen, Z. Zheng, M. Ishaq, G. Liang, F. Ping, T. Chen,J. Tang, Recent progress and perspectives on Sb_2Se_3-based photocathodes for solar hydrogen production via photoelectrochemical water splitting. *J. Energy Chem. 67* **(2021)** 508-523.

[3] K. Li, F. Li, C. Chen, P. Jiang, S. Lu, S. Wang, Y. Lu, G. Tu, J. Guo, L. Shui, Z. Liu, B. Song, J. Tang, One-dimensional Sb_2Se_3 enabling ultra-flexible solar cells and mini-modules for IoT applications. *Nano Energy 86* **(2021)**.

[4] Y. Cao, X. Zhu, J. Jiang, C. Liu, J. Zhou, J. Ni, J. Zhang, J. Pang, Rotational design of charge carrier transport layers for optimal antimony trisulfide solar cells and its integration in tandem devices. *Sol. Energ Mat. Sol. C. 206* **(2020)**.

[5] Z. Li, X. Liang, G. Li, H. Liu, H. Zhang, J. Guo, J. Chen, K. Shen, X. San, W. Yu, R. E. I. Schropp, Y. Mai, 9.2%-efficient core-shell structured antimony selenide nanorod array solar cells.

Nat. Commun. 10 **(2019)** 125.

[6] P. Fan, G. Chen, S. Chen, Z. Zheng, M. Azam, N. Ahmad, Z. Su, G. Liang, X. Zhang, Z. Chen, Quasi-Vertically Oriented Sb_2Se_3 Thin-Film Solar Cells with Open-Circuit Voltage Exceeding 500 mV Prepared via Close-Space Sublimation and Selenization. *ACS Appl. Mater. Interfaces 13* **(2021)** 46671-46680.

[7] Y. Cao, X. Zhu, H. Chen, X. Zhang, J. Zhouc, Z. Hu, J. Pang, Towards high efficiency inverted Sb_2Se_3 thin film solar cells. *Sol. Energ Mat. Sol. C. 200* **(2019)**.

[8] Muhammad Azam, Y. Luo, R. Tang, S. Chen, Z. Zheng, Z. Su, H. Ali, P. Fan, H. Ma, T. Chen, G. Liang, X. Zhang. Organic Chloride Salt Interfacial Modified Crystallization for Efficient Antimony Selenosufide Solar Cells. *ACS Appl. Mater. Interfaces 14* **(2022)** 4276-4284.

[9] Y. Cao, C. Liu, J. Jiang, X. Zhu, J. Zhou, J. Ni, J. Zhang, J. Pang, M. H. Rummeli, W. Zhou, H. Liu, G. Cuniberti, Theoretical Insight into High-Efficiency Triple-Junction Tandem Solar Cells via the Band Engineering of Antimony Chalcogenides. *Solar RRL 5* **(2021)**.

[10] S. Chen, T. Liu, Z. Zheng, M. Ishaq, G. Liang, P. Fan, T. Chen and J. Tang, Recent progress and perspectives on Sb_2Se_3-based photocathodes for solar hydrogen production via photoelectrochemical water splitting. *J. Energy Chem. 67* **(2022)** 508-523.

[11] R. Tang, Z. Zheng, Z. Su, X. Li, Y. Wei, X. Zhang, Y. Fu, J. Luo, P. Fan, G. Liang, Highly efficient and stable planar heterojunction solar cell based on sputtered and post-selenized Sb_2Se_3 thin film. *Nano Energy 64* **(2019)** 103929.

[12] G. Liang, Z. Zheng, P. Fan, J. Luo, J. Hu, X. Zhang, H. Ma, B. Fan, Z. Luo, D. Zhang, Thermally induced structural evolution and performance of Sb_2Se_3 films and nanorods prepared by an easy sputtering method. *Sol. Energ Mat. Sol. C. 174* **(2018)** 263-270.

[13] G. Liang, T. Liu, M. Ishaq, Z. Chen, R. Tang, Z. Zheng, Z. Su, P. Fan, X. Zhang, S. Chen, Heterojunction interface engineering enabling high onset potential in Sb_2Se_3/CdS photocathodes for efficient solar hydrogen production. *Chem. Eng. J. 431* **(2022)** 133359.

[14] X. Wen, C. Chen, S. Lu, K. Li, R. Kondrotas, Y. Zhao, W. Chen, L. Gao, C. Wang, J. Zhang, G. Niu, J. Tang, Vapor transport deposition of antimony selenide thin film solar cells with 7.6% efficiency. *Nat. Commun. 9* **(2018)**.

[15] S. Rijal, D. Li, A. Rasha, C. Xiao, S. Sandip, K. Manoj, J. Michael, C. Jiang, A. Mowafak, Z.

Song, Y. Yan, Templated Growth and Passivation of Vertically Oriented Antimony Selenide Thin Films for High-Efficiency Solar Cells in Substrate Configuration. *Adv. Funct. Mater. 2110032* **(2021)**.

[16] H. Lei, J. Chen, Z. Tan, G. Fang, Review of Recent Progress in Antimony Chalcogenide-Based Solar Cells: Materials and Devices. *Solar RRL 3* **(2019)**.

[17] G. Liang, X. Chen, R. Tang, Y. Liu, Y. Li, P. Luo, Z. Su, X. Zhang, P. Fan, S. Chen, Spark plasma sintering of Sb_2Se_3 sputtering target towards highly efficient thin film solar cells. *Sol. Energ Mat. Sol. C. 211* **(2020)** 110503.

[18] K. J. Tiwari, M. Neuschitzer, M. Espindola-Rodriguez, Y. Sanchez, Z. Jehl, P. Vidal-Fuentes, E. Saucedo, P. Malar, Efficient Sb_2Se_3/CdS planar heterojunction solar cells in substrate configuration with (hk0) oriented Sb_2Se_3 thin films. *Sol. Energ Mat. Sol. C. 215* **(2020)** 110603.

[19] S. Messina, M. T. S. Nair, P. K. Nair, Antimony Selenide Absorber Thin Films in All-Chemically Deposited Solar Cells. *J. Electrochem. Soc. 156* **(2009)** H327-H332.

[20] M. Leng, C. Chen, D.-J. Xue, J. Gong, Y. Liu, K. Li, X. Xiao, G. Wang, J. Tang, Sb_2Se_3 solar cells employing metal-organic solution coated CdS buffer layer. *Sol. Energ Mat. Sol. C. 225* **(2021)**.

[21] Q. Du, B. Li, S. Shi, K. Zhang, Y. Zhang, S. Cheng, Z. Zhou, F. Liu, S. Sun, Y. Sun, W. Liu, Relationship between the intermediate phases of the sputtered Zn(O,S) buffer layer and the conduction band offset in Cd-free Cu(In,Ga)Se_2 solar cells. *Crystengcomm 22* **(2020)** 4416-4426.

[22] F. Larsson, O. Donzel-Gargand, J. Keller, M. Edoff, T. Torndahl, Atomic layer deposition of Zn(O,S) buffer layers for Cu(In,Ga)Se_2 solar cells with KF post-deposition treatment. *Sol. Energ Mat. Sol. C. 183* **(2018)** 8-15.

[23] H. Guo, Z. Chen, X. Wang, Q. Cang, C. Ma, X. Jia, N. Yuan, J. Ding, Significant increase in efficiency and limited toxicity of a solar cell based on Sb_2Se_3 with SnO_2 as a buffer layer. *Journal of Materials Chemistry C 7* **(2019)** 14350-14356.

[24] X. X. Wen, Y. S. He, C. Chen, X. S. Liu, L. Wang, B. Yang, M. Y. Leng, H. B. Song, K. Zeng, D. B. Li, K. H. Li, L. Gao, J. Tang, Magnetron sputtered ZnO buffer layer for Sb_2Se_3 thin film solar cells. *Sol. Energ Mat. Sol. C. 172* **(2017)** 74-81.

[25] M. Saadat, O. Amiri, A. Randar, Optimization of (Zn,Sn)O buffer layer in Cu(In,Ga)Se_2 based solar cells. *Sol. Energy 189* **(2019)** 464-470.

[26] M. Ishaq, S. Chen, U. Farooq, M. Azam, H. Deng, Z. Su, Z. Zheng, P. Fan, H. Song, G. Liang, High Open-Circuit Voltage in Full-Inorganic Sb_2S_3 Solar Cell via Modified Zn-Doped TiO_2 Electron Transport Layer. *Solar RRL 4* **(2020)**.

[27] W. Weihuang, C. Zixiu, W. Huanhuan, L. Jingshan, Y. Zhang, Remarkable Cd-free Sb_2Se_3 solar cell yield achieved by interface band-alignment and growth orientation screening. *J. Mater. Chem. A* **(2021)**.

[28] M. Nakamura, K. Yamaguchi, Y. Kimoto, Y. Yasaki, T. Kato, H. Sugimoto, Cd-Free $Cu(In,Ga)(Se,S)_2$ Thin-Film Solar Cell With Record Efficiency of 23.35%. *Ieee J Photovolt. 9* **(2019)** 1863-1867.

[29] T. Ericson, F. Larsson, T. Torndahl, C. Frisk, J. Larsen, V. Kosyak, C. Hagglund, S. Li, C. Platzer-Bjorkman, Zinc-Tin-Oxide Buffer Layer and Low Temperature Post Annealing Resulting in a 9.0% Efficient Cd-Free Cu_2ZnSnS_4 Solar Cell. *Solar RRL 1* **(2017)** 1700001.

[30] X. Cui, K. Sun, J. Huang, C. Lee, C. Yan, H. Sun, Y. Zhang, F. Liu, M. A. Hossain, Y. Zakaria, L. H. Wong, M. Green, B. Hoex, X. Hao, Enhanced Heterojunction Interface Quality To Achieve 9.3% Efficient Cd-Free Cu_2ZnSnS_4 Solar Cells Using Atomic Layer Deposition ZnSnO Buffer Layer. *Chem. Mater. 30* **(2018)** 7860-7871.

[31] G. Liang, Y. Luo, S. Chen, R. Tang, Z. Zheng, X. Li, X. Liu, Y. Liu, Y. Li, X. Chen, Z. Su, X. Zhang, H. Ma, P. Fan, Sputtered and selenized Sb_2Se_3 thin-film solar cells with open-circuit voltage exceeding 500 mV. *Nano Energy 73* **(2020)**.

[32] X. Li, Z. Su, S. Venkataraj, S. K. Batabyal, L. H. Wong, 8.6% Efficiency CZTSSe solar cell with atomic layer deposited Zn-Sn-O buffer layer. *Sol. Energ Mat. Sol. C. 157* **(2016)** 101-107.

[33] M. Kamruzzaman, L. Chaoping, F. Yishu, A. K. M. F. Ul Islam, J. A. Zapien, Atmospheric annealing effect on $TiO_2/Sb_2S_3/P_3HT$ heterojunction hybrid solar cell performance. *Rsc Advances 6* **(2016)** 99282-99290.

[34] W. Wang, X. Wang, G. Chen, B. Chen, H. Cai, T. Chen, S. Chen, Z. Huang, C. Zhu, Y. Zhang, Promising $Sb_2(S,Se)_3$ Solar Cells with High Open Voltage by Application of a TiO_2/CdS Double Buffer Layer. *Solar RRL 2* **(2018)** 1800208.

[35] D. A. R. Barkhouse, R. Haight, N. Sakai, H. Hiroi, H. Sugimoto, D. B. Mitzi, Cd-free buffer layer materials on $Cu_2ZnSn(S_xSe_{1-x})_4$: Band alignments with ZnO, ZnS, and In_2S_3. *Appl. Phys. Lett.*

100 **(2012)** 193904.

[36] L. Kang, L. Zhao, L. Jiang, C. Yan, K. Sun, B. K. Ng, C. Gao, F. Liu, In situ growth of $CuSbS_2$ thin films by reactive co-sputtering for solar cells. *Mater. Sci. Semicond. Process. 84* **(2018)** 101-106.

[37] T. Minemoto, T. Matsui, H. Takakura, Y. Hamakawa, T. Negami, Y. Hashimoto, T. Uenoyama, M. Kitagawa, Theoretical analysis of the effect of conduction band offset of window/CIS layers on performance of CIS solar cells using device simulation. *Sol. Energ Mat. Sol. C. 67* **(2001)** 83-88.

[38] R. Tang, Z. Zheng, Z. Su, J. Luo, P. Fan, X. Zhang, J. Tang, G. Liang, Heterojunction Annealing Enabling Record Open-Circuit Voltage in Antimony Triselenide Solar Cells. *Adv. Mater.* **(2022)** 2109078.

[39] V. B. Chu, D. Siopa, A. Debot, D. Adeleye, M. Sood, A. Lomuscio, M. Melchiorre, J. Guillot, N. Valle, B. El Adib, J. Rommelfangen, P. J. Dale, Waste- and Cd-Free Inkjet-Printed Zn(O,S) Buffer for $Cu(In,Ga)(S,Se)_2$ Thin-Film Solar Cells. *ACS Appl. Mater. Interfaces 13* **(2021)** 13009-13021.

[40] K. H. Chu, L. Ye, W. Wang, D. Wu, D. K. L. Chan, C. Zeng, H. Y. Yip, J. C. Yu, P. K. Wong, Enhanced photocatalytic hydrogen production from aqueous sulfide/sulfite solution by $ZnO_{0.6}S_{0.4}$ with simultaneous dye degradation under visible-light irradiation. *Chemosphere 183* **(2017)** 219-228.

[41] S. Lu, Y. Zhao, C. Chen, Y. Zhou, D. Li, K. Li, W. Chen, X. Wen, C. Wang, R. Kondrotas, N. Lowe, J. Tang, Sb_2Se_3 Thin-Film Photovoltaics Using Aqueous Solution Sprayed SnO_2 as the Buffer Layer. *Adv. Electron. Mater.4* **(2018)** 1700329.

[42] X. Cui, K. Sun, C.-Y. Lee, C. Yan, H. Sun, Y. Zhang, F. Liu, M. Green, B. Hoex, X. Hao, Ieee, ALD ZnSnO buffer layer for enhancing heterojunction interface quality of CZTS solar cells. In *2018 Ieee 7th World Conference on Photovoltaic Energy Conversion*, 2018; pp 1511-1513.

[43] Y. Luo, R. Tang, S. Chen, J. Hu, Y. Liu, Y. Li, X. Liu, Z. Zheng, Z. Su, X. Ma, P. Fan, X. Zhang, H. Ma, Z. Chen, G. Liang, An effective combination reaction involved with sputtered and selenized Sb precursors for efficient Sb_2Se_3 thin film solar cells. *Chem. Eng. J. 393* **(2020)** 124599.

[44] M. Ishaq, H. Deng, S. Yuan, H. Zhang, J. Khan, U. Farooq, H. Song, J. Tang, Efficient Double Buffer Layer $Sb_2 (Se_xS_{1-x})_3$ Thin Film Solar Cell Via Single Source Evaporation. *Solar RRL 2* **(2018)** 1800144.

[45] J. Lee, T. Enkhbat, G. Han, M. H. Sharif, E. Enkhbayar, H. Yoo, J. H. Kim, S. Kim, J. Kim, Over 11 % efficient eco-friendly kesterite solar cell: Effects of S-enriched surface of $Cu_2ZnSn(S,Se)_4$ absorber and band gap controlled (Zn,Sn) O buffer. *Nano Energy 78* **(2020)** 105206.

[46] G. Liang, M. Chen, M. Ishaq, X. Li, R. Tang, Z. Zheng, Zh. Su, P. Fan, X. Zhang, S. Chen, Crystal Growth Promotion and Defects Healing Enable Minimum Open-Circuit Voltage Deficit in Antimony Selenide Solar Cells. *Adv. Sci.* **(2022)** 2105142.

[47] X. Hu, J. Tao, G. Weng, J. Jiang, S. Chen, Z. Zhu, J. Chu, Investigation of electrically-active defects in Sb_2Se_3 thin-film solar cells with up to 5.91% efficiency via admittance spectroscopy. *Sol. Energ Mat. Sol. C. 186* **(2018)** 324-329.

[48] Y. Wang, J. Li, Y. Chen, J. Zhou, J. Zhang, W. Mao, S. Zheng, Y. Pan, Y. Liu, K. Dai, X. Hu, J. Tao, G.-E. Weng, J. Jiang, S. Chen, J. Chu, Effects of working pressure and power on photovoltaic and defect properties of magnetron sputtered Sb_2Se_3 thin-film solar cells. *Appl. Opt. 59* **(2020)** 948-954.